



# Experimental investigation of blade tip vortex behavior in the wake of asymmetric rotors

Aliza Abraham<sup>1</sup> · Thomas Leweke<sup>1</sup>

Received: 5 January 2023 / Revised: 31 March 2023 / Accepted: 22 April 2023 / Published online: 23 May 2023  
© The Author(s), under exclusive licence to Springer-Verlag GmbH Germany, part of Springer Nature 2023

## Abstract

Wakes behind rotors such as wind turbines, propellers, and helicopters can have detrimental effects on downstream structures including increased structural loading. These wakes are characterized by helical vortices shed from the blade tips, which are subject to instabilities that cause the vortices to break down, reducing the strength of the wake. One type of instability, vortex pairing, can be triggered by introducing a slight asymmetry to the rotor. The current study investigates the effectiveness of different types of rotor asymmetries at triggering the pairing instability through an experimental campaign involving 14 rotor configurations. The leapfrogging distance, or the point where adjacent vortex loops swap positions, is used as a metric to compare the different types of asymmetries. For all cases tested, leapfrogging occurs between 4.1 and 1.8 rotor radii downstream of the rotor for the baseline and most perturbed configurations, respectively. Even a small perturbation of 6% of the vortex spacing reduces the leapfrogging distance by 25% relative to the baseline configuration. Some of the most interesting similarities and differences between cases are discussed in more detail, including the analogy between azimuthal and axial displacements, the importance of perturbation direction, and the effects of blade devices such as winglets and fins on the vortex system. The findings of the current study can be used to design rotors that passively accelerate wake recovery, mitigating detrimental effects on downstream structures.

## 1 Introduction

Rotors, such as those found on wind turbines, helicopters, and propellers, shed wakes which are characterized by helical tip vortices. These wakes, and the tip vortices in particular, can have detrimental effects on downstream structures. For example, wind turbine wakes with coherent tip vortices are known to increase the structural loading on downstream turbines within a wind farm, relative to fully turbulent wakes (Sørensen 2011). In addition, tip vortices prevent mixing between the lower-speed flow within the wake and the freestream flow outside (Lignarolo et al. 2015). When downstream turbines are located within this low-speed wake, substantial power losses up to 40% have been observed (Lee and Fields 2021). Several methods have been proposed for the mitigation of detrimental wake effects by modifying the

whole wake flow through induction control, yaw control, and individual pitch control (see Meyers et al. (2022) for an overview of wind farm flow control methods). The current study targets the tip vortices in particular, investigating a passive flow control method for the acceleration of tip vortex breakdown.

Helical vortex systems are subject to instabilities which can cause the vortices to break down. These instabilities fall into two categories: short-wave and long-wave (Leweke et al. 2014). Short-wave instabilities are characterized by perturbations smaller than the vortex core size, and long-wave instabilities, which are the focus of the current investigation, occur when the vortex displacements are large relative to the core size. These long-wave instabilities lead to pairing and leapfrogging, or the swapping of axial positions, between adjacent vortex loops. This pairing instability of helical vortex systems has been studied theoretically for decades, since Widnall (1972) derived the growth rates of different wavenumber perturbations for a single helical vortex filament. Gupta and Loewy (1974) and Okulov and Sørensen (2007) extended this analysis to systems of multiple interdigitated helical vortices.

---

✉ Aliza Abraham  
aliza.abraham@univ-amu.fr  
Thomas Leweke  
thomas.leweke@cnsr.fr

<sup>1</sup> IRPHE, Aix-Marseille Université CNRS, Centrale Méditerranée, 13384 Marseille, France

Several studies have also investigated the pairing instability in helical vortex systems using numerical methods. Bhagwat and Leishman (2000) used a free-vortex method to characterize the stability of a helicopter rotor wake, observing several unstable modes including tip vortex pairing. Ivanell et al. (2010) and Sarmast et al. (2014) calculated the growth rates of wind turbine wake perturbations at different frequencies, first by modeling one-third of the rotor under the assumption of azimuthal symmetry, then by modeling the whole rotor to highlight the importance of asymmetric modes. To test a practical method of generating unstable perturbations, Huang et al. (2019) and Marten et al. (2020) modeled wind turbine rotors with flaps, showing that vortex pairing could be induced even with small actuation amplitudes. More recent studies have explored additional practical aspects of tip vortex instabilities in wind turbine wakes, including the excitation of perturbations using existing control actuators such as blade pitch and rotor speed (Brown et al. 2022), the effect of wave-induced oscillations for floating offshore turbines (Kleine et al. 2022), and the impact of atmospheric shear and thermal stratification on perturbation evolution (Hodgkin et al. 2022).

Helical vortex pairing has been observed experimentally since Alfredsson and Dahlberg (1979) visualized leapfrogging tip vortices in the wake of a model wind turbine using smoke, though detailed experimental characterizations of the phenomenon are scarce. Felli et al. (2011) investigated the dependence of the pairing instability evolution in the wake of a propeller on spacing between adjacent vortex loops, finding that leapfrogging occurs earlier when such spacing is reduced. Nemes et al. (2015) confirmed this finding and showed that the measured growth rates of the instability matched the expected theoretical values for the wavenumbers tested. To understand the effect of the pairing instability on wake mixing and recovery, [2] computed the kinetic energy transport into the wake of a rotor with blades pitched at two slightly different angles. They showed that this kinetic energy transport increases substantially after leapfrogging occurs and the tip vortices break down. Quaranta et al. (2015) characterized vortex geometry and instability growth rates for a single helix in the wake of a one-bladed rotor, finding good agreement with theoretical modes. Extending this work to a double helix, Quaranta et al. (2019) explored both local and global vortex pairing. Local pairing occurs when the azimuthal wavenumber of the perturbation is nonzero and the distance between adjacent loops varies along the azimuth. Global pairing is characterized by a zero wavenumber perturbation where one of multiple interlaced helices is shifted relative to the other(s), leading to uniform spacing along the azimuth. As demonstrated by Quaranta et al. (2019), global pairing can be triggered by introducing an asymmetry to the rotor generating the helical vortices.

The current study experimentally investigates global pairing in the helical vortex system in the wake of an asymmetric three-bladed rotor. The three-bladed configuration is more relevant to applications such as wind turbines. Furthermore, the addition of a third helix substantially increases the complexity of the vortex interactions. The paper is structured as follows: Sect. 2 describes the experimental setup, including the design of the three-bladed rotor, the different types of asymmetry tested, and the measurement techniques used in the study. Section 3 presents the results of the comparison between different types of asymmetry and discusses some of the most interesting findings in more detail. Finally, Sect. 4 delivers the key conclusions of the study.

## 2 Experimental methods

### 2.1 Baseline configuration

Experiments were conducted in a recirculating free-surface water channel with a test section of dimensions 150 cm  $\times$  38 cm  $\times$  50 cm (length  $\times$  width  $\times$  height). A three-bladed rotor with a radius of  $R = 9$  cm was mounted on a 1.5 cm diameter shaft, driven by a stepper motor at  $f = 3$  Hz (see Fig. 3 below). The flow in the channel had a uniform velocity of  $U_0 = 56$  cm/s, giving a tip speed ratio of  $\lambda = 2\pi Rf/U_0 = 3.0$ . The airfoil cross section used for the rotor blades was the NACA2414, which performs reliably at low Reynolds numbers (Selig et al. 1996) and is sufficiently thick for fabrication using additive manufacturing. This thickness, along with the stiffness of the manufacturing material, Formlabs Rigid 10K resin (flexural modulus of 9 GPa after UV curing (Formlabs 2022)), prevent any significant blade deflections during rotor operation. The blade chord ( $c$ ) and twist ( $\phi$ ) for the outer 50% of the radius were determined using the Glauert method for wind turbines (Glauert 1935), while the inner 50% was adapted to ensure a smooth connection to the rotor hub, which had a radius of 1.25 mm (Fig. 1a). Note that these blades were designed to generate strong tip vortices for the investigation of helical vortex dynamics; the rotor was not optimized for power extraction.

The rotor hub was designed to allow the removal of each blade individually so that rotor asymmetry could be introduced by replacing one or two blades with slightly modified ones. Such modifications are discussed in more detail in 2.2. Each blade was manufactured with a flat base that attached to the hub with screws and a square peg that nests into the corresponding square hole in the hub (Fig. 1b). These features ensured each blade was aligned with the hub consistently each time it was replaced. Because the helical vortex system is highly sensitive to perturbations, the baseline case had to be sufficiently symmetric to prevent the instability

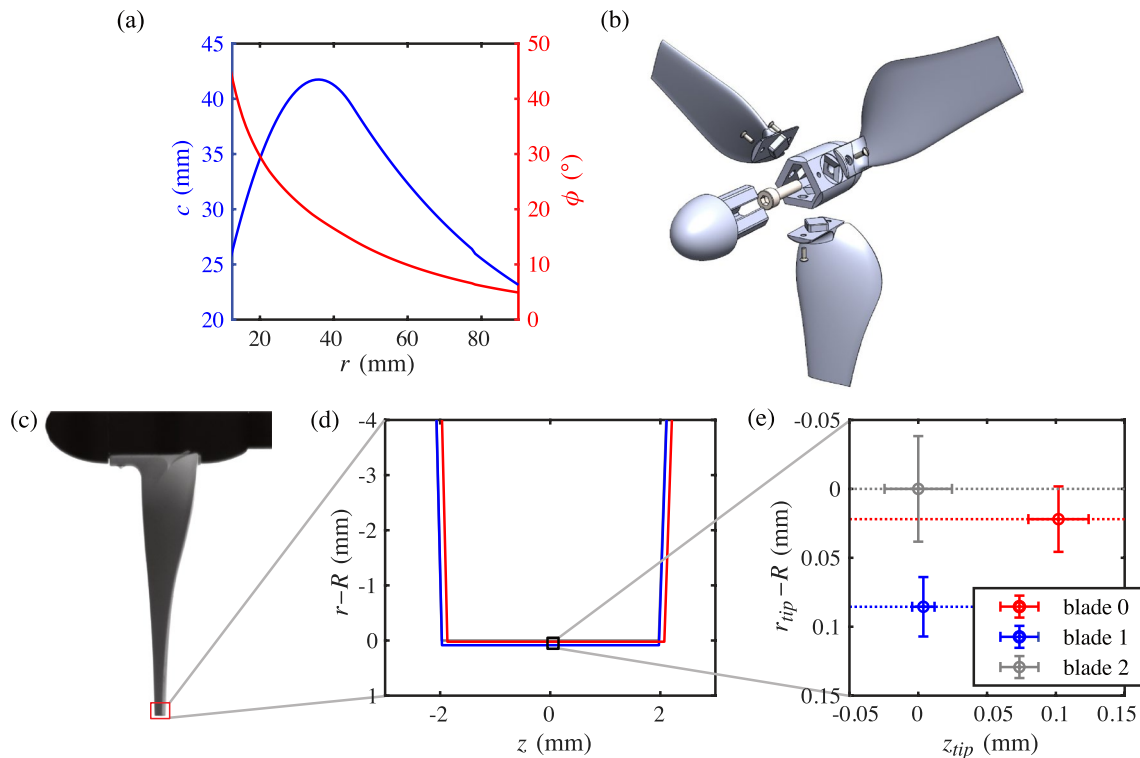


**Fig. 1** **a** Chord ( $c$ ) and twist angle ( $\phi$ ) of the baseline rotor blades. **b** Exploded view of the rotor showing how the blades attach to the hub. The white screw in the center connects the rotor to the shaft. **c** Sample image of one rotor blade used to identify the blade tip position. The red box around the blade tip indicates the region shown in **(d)**,

where the colored outlines representing the edges of the tips of the three blades from the images are compared. The black square marks the position of the inset in **(e)**, which shows a closer view of the deviation between the blade tip center locations ( $r_{tip}, z_{tip}$ ), indicated by the circles with error bars

from appearing until far downstream. The tip positions were measured using a camera synchronized with the rotor rotation that captured images of each blade when it was pointing directly downwards (sample image shown in Fig. 1c). The maximum deviations in both the axial and radial directions between the positions of the three blade tips were measured to be around 0.1% of  $R$  for the baseline rotor (Fig. 1d).

### 2.2 Rotor modifications

In addition to the baseline blade, 11 other slightly modified blades were designed and manufactured. These modified blades were designed to perturb the tip vortex position ( $r_{tip}, z_{tip}$ ) in different directions and by different amounts. For example, a blade that was elongated in the radial direction,  $r$ , and deflected in the axial direction,  $z$ , as shown in Fig. 2a, would displace the tip vortex to the new tip position of the modified blade. Seven blades of this type were manufactured, with the tip location of each displaced in the  $r$  and  $z$  directions by different magnitudes and signs. For each of these cases, radial deformations were implemented by linearly extrapolating (for  $+r$ ) or truncating (for  $-r$ ) the chord and twist of the baseline blade. Axial deformations

were implemented such that the quarter chord line followed the fourth-order polynomial shape predicted by beam theory for a cantilevered beam under a distributed load. Note that the magnitudes of the perturbations are presented as percentages of  $h$ , the spacing between adjacent loops of the tip vortex helix, which is measured in the baseline rotor wake (Sect. 3.1).

The blade shown in Fig. 2b displaced the vortex in the azimuthal direction, i.e., in the direction of the rotor rotation. In this case, the quarter chord line of the blade was rotated about the hub axis by  $5.7^\circ$ . Blades featuring added devices, such as a winglet (Fig. 2c) and a fin (Fig. 2d), were also manufactured. The winglet was designed by linearly extrapolating the chord and twist of the baseline blade, then adding a  $45^\circ$  bend at  $r = R$ , such that the tip of the winglet was located at  $(r, z) = (R + 0.13h, 0.11h)$ . The fin was designed based on the findings of Schröder et al. (2021), which showed that two vortices are shed in this configuration, one at the tip of the blade and one at the tip of the fin. These vortices merge to form a larger, more diffuse vortex between the position of the fin and tip vortices. The higher the angle of attack of the fin, the more the merged vortex is displaced away from the tip position, so the fin in the

current study was designed with an angle of attack of  $16^\circ$ . In addition, the trailing edge of the fin was positioned at the trailing edge of the blade to minimize the distance between the vortices and promote merging, following the results presented by Schröder et al. (2022). The quarter chord position of the fin was located at  $(r, z) = (R - 0.13h, -0.12h)$ . Finally, one blade was designed with a decrease in angle of attack of  $1^\circ$  relative to the baseline blade to reduce the circulation of the resulting tip vortex. Based on the lift curve for the NACA2414 airfoil, such a decrease in angle of attack was expected to reduce the lift coefficient by 11%, yielding a corresponding decrease in tip vortex circulation of 11%. Table 1 lists all rotor configurations tested experimentally. Note that the listed blade tip locations are measurements obtained from images of the blades, as described for the baseline rotor in Sect. 2.1. The tip positions of the modified blades deviated slightly from their design conditions by  $\sim 0.01h - 0.02h$  due to some tolerance in the blade mounting mechanism. The designed configurations were determined based on the results of the point vortex-based wake model described by Abraham et al. (2023).

### 2.3 Measurement and evaluation techniques

Multiple techniques were used to compare the effects of different rotor asymmetries on the wake. To visualize the three-dimensional behavior of the tip vortices, a fluorescein dye paste was painted on the tips of the rotor blades outside of the water. The rotor then began spinning and was lowered into the channel. The test section volume was illuminated with two blue LED panels, as depicted in Fig. 3, causing

the dye entrained in the tip vortices to fluoresce. The tip vortices appear as green interlaced helices in the volumetric visualization images. To track the positions of the vortex centers over time, the LED panels were removed and a laser sheet was used to illuminate a cross section of the wake in the plane of the shaft. Because the shaft blocked the light from reaching the upper half of the test section, only the bottom part of the cross section is visible. This occlusion is acceptable because the global tip vortex pairing behavior investigated in the current study is independent of azimuthal position.

The distance from the rotor plane where leapfrogging, or the swapping of axial positions between two adjacent vortex loops, occurs ( $z_c$ ) is used to compare the effectiveness of different rotor asymmetries at perturbing the vortex system in the wake. A shorter leapfrogging distance indicates a more effective perturbation. This metric is used because it is an indicator of the perturbation evolution speed and it is easily identified from the experimental data. In addition, the point of leapfrogging coincides with the location of minimum distance between two adjacent vortices, corresponding to a greater likelihood of vortex breakdown due to short-wave instabilities (Lewke and Williamson 1998). In time averages of the volumetric tip vortex visualizations, the leapfrogging position can be identified as the location of maximum radial separation between the inner and outer wake envelopes, as seen in Fig. 4a. Cross-sectional visualization images were used to obtain a more precise leapfrogging location by tracking the positions of the vortex centers over time (Fig. 4b). The vortex tracks were obtained using motion-based multiple object tracking in MATLAB. Fig. 4c

**Table 1** Table listing all rotor configurations tested, including the label which is used to refer to each case throughout the paper, a description of the rotor modification in words, and the coordinates of the modified blade tip

Label	Description	Blade tip location		
		$(r_{tip} - R)/h$	$z_{tip}/h$	$\theta_{tip}$
B	Baseline	0	0	0
C	Radial extension	0.06	- 0.01	0
D	Axial deflection	0	0.05	0
E	Radial extension	0.08	0.01	0
G	Axial deflection	0	0.08	0
H	Radial extension and axial deflection	0.06	0.05	0
K	Radial extension and axial deflection	0.05	- 0.06	0
L	Radial shortening and axial deflection	- 0.06	- 0.07	0
A	Azimuthal shift	0	0	$5.7^\circ$
W	Winglet	0.13	0.11	0
F	Fin	0 (blade), - 0.13 (fin)	0 (blade), - 0.12 (fin)	0 (blade), 0 (fin)
P	Pitch change (angle of attack reduced by $1^\circ$ )	0	0	0
HL	Two blades changed, one to H and one to L	0.05 (H); - 0.06 (L)	0.05 (H); - 0.07 (L)	0 (H); 0 (L)
WF	Two blades changed, one to W and one to F	0.14 (W); 0 (F, blade), - 0.14 (F, fin)	0.11 (W); 0 (F, blade), - 0.13 (F, fin)	0 (W); 0 (F, blade), 0 (F, fin)

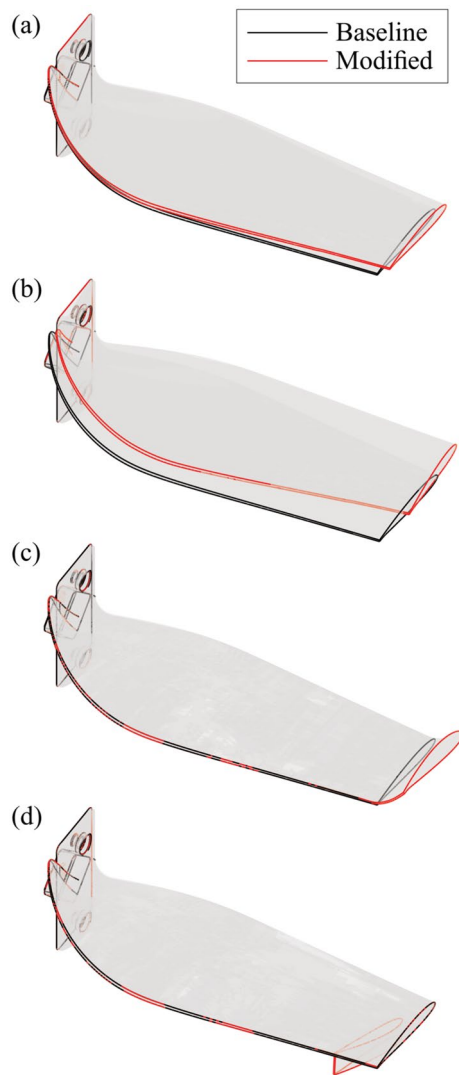


**Fig. 2** Examples of modified blades used to introduce rotor asymmetry, with **a** a perturbation in the positive radial and axial directions (H in Table 1), **b** a perturbation in the azimuthal direction (A in Table 1), **c** a winglet added to the blade tip (W in Table 1), and **d** a fin on the pressure side (F in Table 1)

and **d** shows example time series of the axial and radial positions, respectively, of the average positions of the vortices shed from the three rotor blades. Time ( $t$ ) is normalized by the vortex spacing and circulation, such that  $t^* = t\Gamma/(2h^2)$ , where the tip vortex circulation  $\Gamma$  is measured in the wake of the baseline rotor (Sect. 3.1). The time when the first vortex is shed from the rotor (i.e., at  $z = 0$ ) is defined as  $t^* = 0$ . The distances are normalized by vortex spacing,  $h$ , based on Quaranta et al. (2015). In the radial direction, the wake mean expansion  $R_w(z)$ , computed as described in Sect. 3.1, is subtracted from the trajectory. The leapfrogging location is identified as the point where the axial tracks of two vortices cross, as indicated by the black line in Fig. 4c. The vortex trajectories shown in Fig. 4 correspond to configuration E

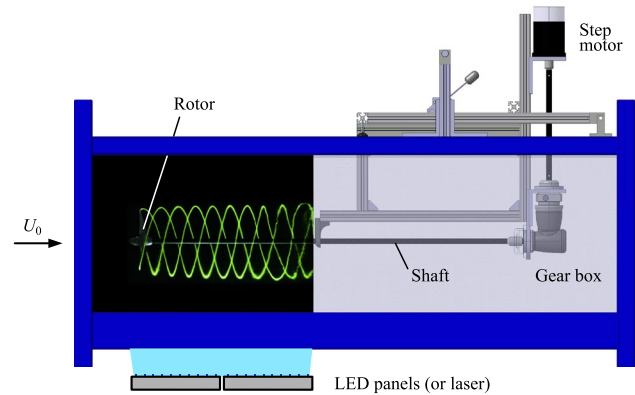


**Fig. 3** Schematic of the water channel test section, including the components powering and supporting the rotor, the positioning of the light source for vortex visualization, and a sample volumetric visualization image of the tip vortices in the rotor wake

in Table 1, but they exhibit features observed in all cases tested in the current study, including two vortices moving in opposite radial directions, then crossing in the axial direction at the point of maximum radial separation. This behavior is characteristic of the leapfrogging phenomenon.

Particle Image Velocimetry (PIV) was used to obtain wake velocity fields and tip vortex properties. The raw images were obtained by seeding the water channel with 10- $\mu$ m-diameter silver-coated hollow glass spheres and illuminating the plane of the shaft with a 532 nm-wavelength, double-pulsed Nd:YAG laser. The pulse spacing was 2 ms. The camera and laser were triggered by the rotor and synchronized at 4.5 Hz so that an image was captured every  $4/3$  rotation. With this timing, the vortices shed from all three blades could be captured in a single acquisition. Each acquisition consisted of 900 image pairs, corresponding to 300 pairs per vortex. For the baseline rotor, this process was repeated 12 times to capture 36 phases of the rotation. These images were processed with an in-house MATLAB PIV code (Meunier and Leweke 2003). First, a  $64 \times 64$  pixel correlation window with 50% overlap was used for several passes employing window shifting and deformation, and a final pass was conducted with a  $32 \times 32$  pixel window, also with 50% overlap.

## 3 Results

### 3.1 Baseline wake characterization

The flow in the wake of the baseline rotor is first characterized using PIV data. The mean velocity field shows a strong deficit in the wake, as expected for a rotor operating in the turbine regime (Fig. 5a). A slight acceleration is also observed outside of the wake due to flow blockage in

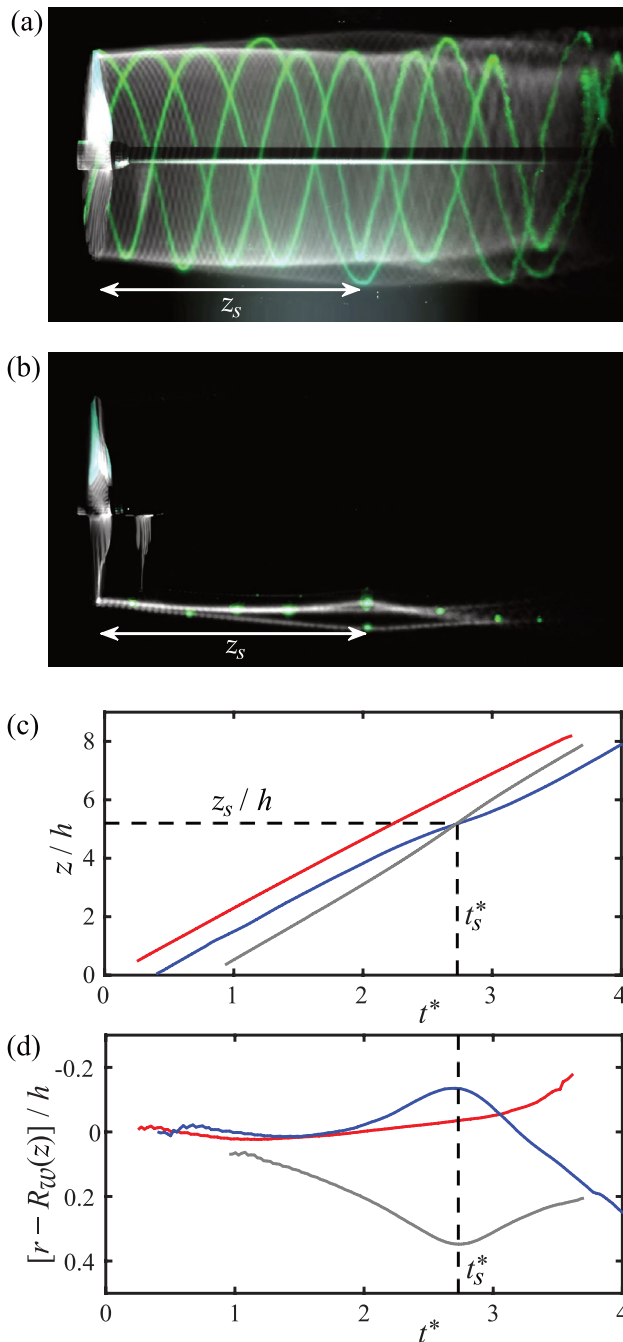


**Fig. 4** **a** Time-average of volumetric visualization images, with one image brighter and in green. **b** Time-average of cross-sectional visualization images, with one image brighter and in green. In both, the leapfrogging distance,  $z_s$ , is indicated by the white arrow. Vortex trajectories in the **c** axial and **d** radial directions obtained from tracking the vortex cross-sections over time. The dimensionless time ( $t_s^*$ ) and location ( $z_s/h$ ) where leapfrogging occurs are indicated by the dashed lines. All panels show results for configuration E in Table 1

the channel. Figure 5b presents an example phase-averaged vorticity field corresponding to a rotational phase of  $60^\circ$ . Tip vortices with negative vorticity are clearly visible at  $r/R \sim 1$ .

Strong blade root vortices are not observed for two reasons. First, as explained in Sect. 2.1, the inner 50% of the blade is modified from the original Glauert design, causing positive vorticity to be shed gradually rather than all at once in the form of a root vortex. Second, the boundary layer generated by the rotor shaft contains negative vorticity, which partly neutralizes the positive vorticity at the blade root, as described by Quaranta et al. (2019).

The coordinates of the center of each tip vortex were manually determined from the vorticity phase averages. From these coordinates, the wake radius ( $R_w/R$ ) and vortex spacing ( $h/R$ ) were determined. Because of the slight residual asymmetry of the baseline rotor, the vortices shed from the three blades follow different trajectories. The geometric wake parameters were determined from the average of these three trajectories. The wake radius shows an initial increase characteristic of wind turbine rotor wake expansion, with a plateau around  $R_w/R = 1.10 \pm 0.02$ , corresponding to  $R_w = (9.9 \pm 0.2)$  cm (Fig. 5c). The vortex spacing decreases slightly within the first  $R$  downstream of the rotor, then remains at  $h/R = 0.52 \pm 0.01$ , or  $h = (4.72 \pm 0.09)$  cm, for the remainder of the wake (Fig. 5d). To calculate the circulation of each tip vortex, line integrals of the azimuthal (in the local vortex reference frame) velocity were computed along circles of radius  $h/3$ , chosen to encompass as much of the tip vortex vorticity as possible without including trailing vorticity shed from a different blade, as shown in Fig. 5b. The axial evolution of the tip vortex circulation for the three blades is presented in Fig. 5d. Vortices shed from all three blades exhibit regions of relatively constant circulation at the beginning of the wake until  $z \sim 1R$ , after which the values decrease slowly for the remainder of the imaging region. This decrease may be due to the detrainment of vorticity from the constant-radius integration area used for the determination of the circulation, from the interaction with neighboring vortices and/or the inner vorticity layers. To characterize the circulation of the tip vortices without these effects, the mean of the circulation between  $0 < z/R < 1$  is used, yielding values of  $\Gamma_0 = (168 \pm 2)$   $\text{cm}^2/\text{s}$ ,  $\Gamma_1 = (163 \pm 2)$   $\text{cm}^2/\text{s}$ , and  $\Gamma_2 = (164 \pm 2)$   $\text{cm}^2/\text{s}$  for each of the three blades. The average of the three values ( $\Gamma = 165$   $\text{cm}^2/\text{s}$ ) is used for the non-dimensionalization of time.

### 3.2 Leapfrogging distance comparison

The effect of different rotor asymmetries is now compared for all cases tested. Figure 6 shows the leapfrogging distance for each case, calculated using the tracked tip vortex positions as described in Sect. 2.3. The cases are labeled according to Table 1. Overall, the leapfrogging distance ranges from  $z_s/R = 4.1$  for the baseline case to  $z_s/R = 1.8$  for the most perturbed case where one blade is replaced with blade W (winglet) and another is replaced with blade F (fin).

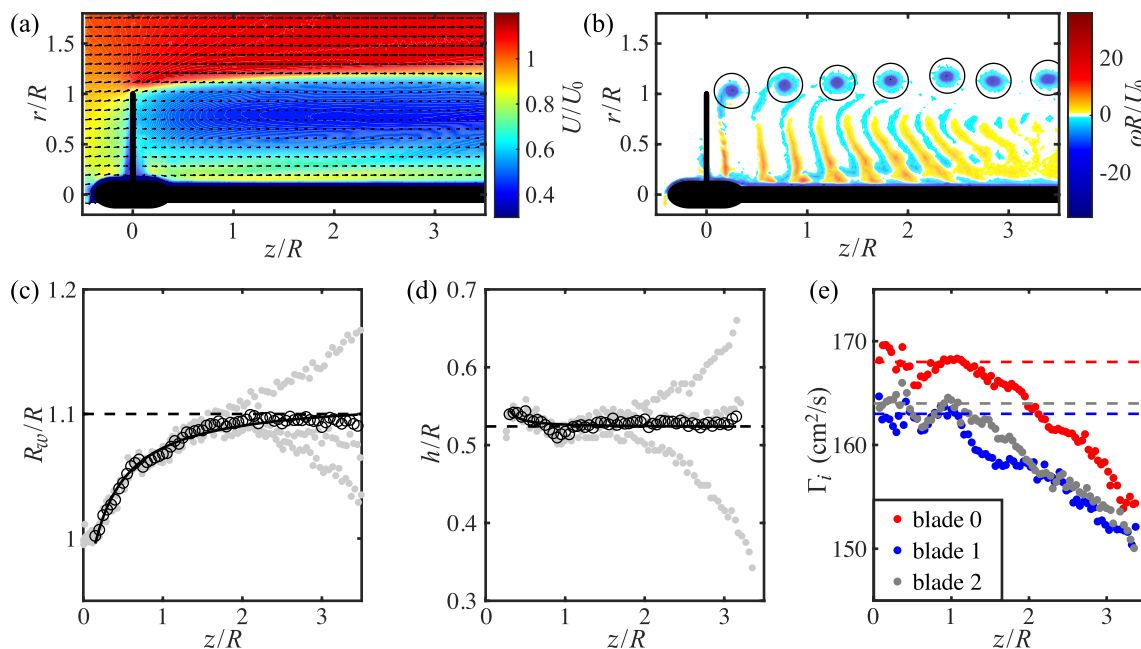


**Fig. 5** **a** Mean velocity field in the wake of the baseline rotor, averaged over 36 rotation phases. The color represents the normalized streamwise velocity, and the arrows indicate the direction. The displayed vector spacing is 1/10 of the actual resolution for readability. **b** Phase-averaged vorticity field in the wake of the baseline rotor corresponding to a rotation phase of 60°. The black circles around the tip vortices represent the lines used to calculate their circulation. **c** Axial evolution of the wake radius normalized by rotor radius. The gray points represent the position of each vortex, the open black circles are the mean at each axial location, and the solid black line is the

fit of the mean points to a trend line that asymptotically approaches a constant value (dashed line). **d** Axial evolution of tip vortex spacing normalized by rotor radius. The gray points represent the spacing between adjacent vortices, the open black circles are the mean at each axial location, and the solid black line is the trend line. **e** Axial evolution of tip vortex circulation for the vortices shed from each of the three blades. The points represent the circulation values of each vortex, with the color indicating the blade from which it was shed. The dashed lines show the mean values of  $\Gamma_i$  ( $i = 0,1,2$ ) between  $0 < z/R < 1$  for each blade

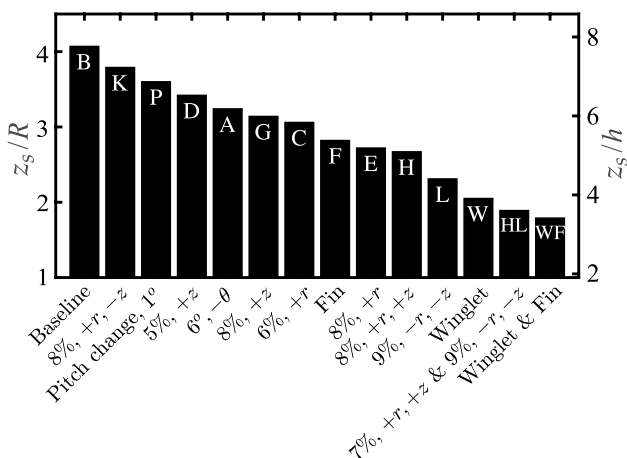


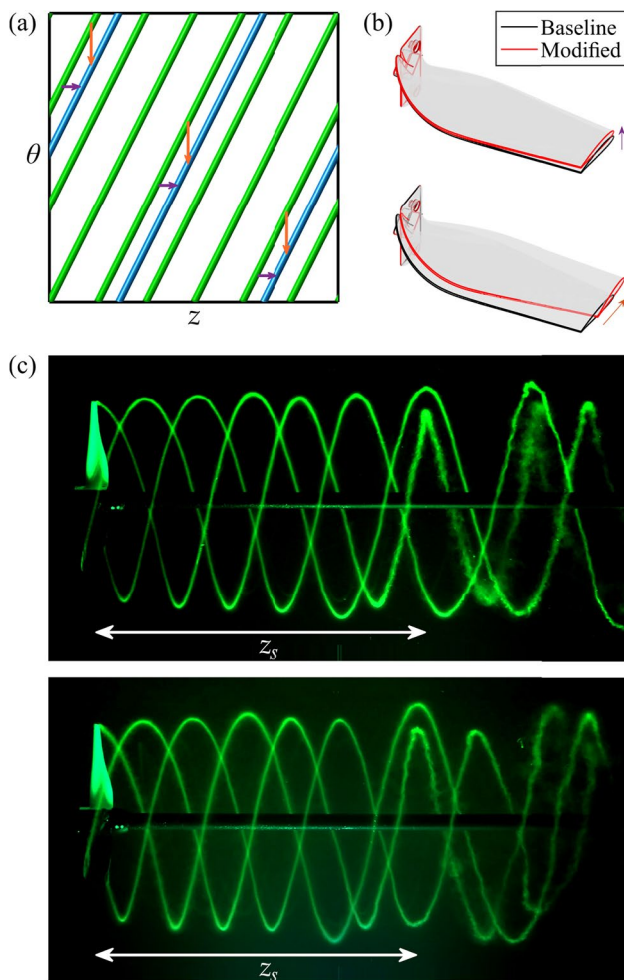
**Fig. 6** Comparison of leapfrogging distance ( $z_s$ ) for all cases tested in the current study, normalized by both rotor radius ( $R$ ) and vortex spacing ( $h$ ). The white letters on the bars correspond to the case labels as defined in Table 1

The values of  $z_s$  measured in this study show the substantial impact that even small asymmetries have on the rotor wake, particularly for the baseline case with asymmetries of

$\sim 0.1\%$  of  $R$ . The subsequent analysis focuses on explaining the key differences and similarities between a few of the other cases tested in this study.

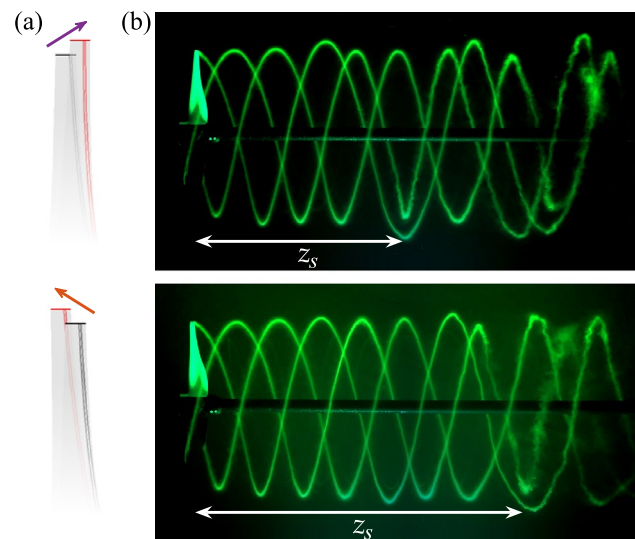
### 3.2.1 Azimuthal and axial equivalence

Figure 6 shows that the leapfrogging distance resulting from a 5.7° azimuthal tip displacement (blade A,  $z_s/R = 3.2$ ) is nearly equivalent to that resulting from an axial displacement of 0.05h (blade D,  $z_s/R = 3.4$ ). The similarity between these two cases is due to the helical geometry of the tip vortex system. Figure 7a presents the developed plan view of the helical vortex system, with the horizontal axis representing the axial direction and the vertical axis representing the azimuthal direction. This view shows that a displacement of the vortex system along the axial direction (purple arrows) is equivalent to a displacement along the azimuthal direction (orange arrows). Because a full 360° rotation of the rotor causes the vortices to propagate  $3h$  in the axial direction, an axial displacement of  $h$  is equivalent to 120° of rotation. Therefore, a blade with an azimuthal perturbation of 6° was designed to be equivalent to an axial perturbation of 0.05h



**Fig. 7** **a** Developed plan view of the helical vortex system. The original vortices are in green and the displaced vortex is in blue. Purple arrows represent an axial displacement, and orange arrows show the equivalent azimuthal displacement. **b** Modified blades used to induce (top) an axial displacement of  $0.05h$  (D in Table 1) and (bottom) an azimuthal displacement of  $5.7^\circ$  (A in Table 1). The purple and orange arrows indicating the directions of the perturbations correspond to those in (a). **c** Volumetric visualization images of the wakes of the rotors with one blade replaced with those shown in (b), with the white arrows indicating the leapfrogging distance,  $z_s$ , for each case

(Fig. 7b). Figure 7c shows that when one of the rotor blades is replaced with each of these modified blades, the resulting wake is nearly identical up to the point of leapfrogging. Downstream of  $z_s$ , the vortex dynamics differ between the two cases. This discrepancy is attributed to the fact that blade D is deformed slightly along the entire length due to the axial deflection, modifying the circulation distribution along the blade and inside the wake. Due to the nonlinearity of the vortex system, these small differences are magnified further downstream.



**Fig. 8** **a** Modified blades used to induce vortex perturbations along (top) the positive strain direction (H in Table 1), indicated by the purple arrow, and (bottom) the negative strain direction (K in Table 1), indicated by the orange arrow, of the co-rotating vortex system. Only the blade tips are shown for clarity. The resulting volumetric visualizations of the wakes of the rotors modified with these blades are shown in (b), highlighting the large difference in leapfrogging distance,  $z_s$

### 3.2.2 Directional effects

Another key insight gained from Fig. 6 is the strong dependence of the leapfrogging distance on the direction of the perturbation. In particular, blades K and H both feature a displacement of the same magnitude, with extensions in the radial direction, but K has a negative axial deflection while H has a positive one. Just changing the sign of the axial deflection puts K and H on almost opposite ends of the range of  $z_s$  values, with  $z_s/R = 3.8$  and  $z_s/R = 2.7$ , respectively. The cause of this difference is related to the behavior of co-rotating vortex systems, which generate a strain field with elliptic streamlines oriented at  $45^\circ$  relative to the axis connecting the vortices (Lewke et al. 2016). When one vortex is perturbed along the direction of positive strain, as is the effect of blade H shown at the top of Fig. 8a, the strain field continues to push the vortex away from its initial position. On the other hand, when one vortex is perturbed along the direction of negative strain, as for blade K shown at the bottom of Fig. 8a, the strain field pushes the vortex back toward its initial position. Therefore, a vortex displacement along the direction of positive strain causes the instability to evolve more quickly than a displacement in the negative strain direction, leading to a shorter leapfrogging distance. The difference in leapfrogging distance between these two cases is clear in the volumetric wake visualizations shown in Fig. 8b. In configuration HL, two of the blades induce



perturbations along the positive strain direction, further reducing the leapfrogging distance.

### 3.2.3 Blade devices

The addition of a winglet to the tip of one of the blades (blade W) strongly displaces the tip vortex. The winglet changes the blade tip location the most of all of the modified blades (Fig. 9a), and it displaces the vortex along the positive strain direction, as discussed in Sect. 3.2.2. Therefore, it causes the strongest perturbation to the vortex system and the shortest leapfrogging distance of all of the configurations with only one blade changed (Fig. 9b). Previous studies have shown that, for certain winglet designs, a secondary vortex is formed at the blade bending location at the base of the winglet (Gerontakos and Lee 2006; Ostovan et al. 2019). Depending on the cant angle of the winglet, this secondary vortex may merge with the vortex formed at the winglet tip, with the final vortex residing somewhere between the positions of the two initial vortices. In the current study, no vortex is observed at the base of the winglet due to the smooth transition between the main blade and the winglet. The vorticity field captured 60° after the winglet blade has crossed the imaging plane, presented in Fig. 9c, shows a single vortex downstream of the winglet tip location.

On the other hand, the blade with the fin (blade F) is observed to generate two vortices, one at the blade tip and one at the fin tip. This feature can be seen most clearly in the vorticity field shown in Fig. 9c, where the vortex most recently shed from the fin blade has two distinct lobes. Note that the resolution of the present PIV data is insufficient for accurate measurements of the vortex core size. However, consistent with the findings of Schröder et al. (2021), the two lobes appear to merge, and the merged vortex continues to propagate downstream at a location between the two initial positions. Note that this merged vortex position is also along the positive strain direction. Although the merged vortex does not look significantly different from the vortices shed from the baseline blades in the vorticity field, it appears more diffuse in the volumetric visualization (Fig. 9b). The results of Schröder et al. (2021) show that the core of the merged vortex is larger than that of the vortices shed from the baseline blade, though this observation cannot be confirmed using the current data, due to the lack of resolution in the vortex core regions. Because of the large vortex displacements caused by both the winglet and the fin, the rotor configuration that uses both of these blades (configuration WF) generates the wake with the shortest leapfrogging distance of all configurations tested.

In addition to vortex displacement, Fig. 9d presents the circulation of the vortices shed from all three blades in both configurations. Note that there are fewer data points than in the circulation plot in Fig. 5e, as fewer phases of

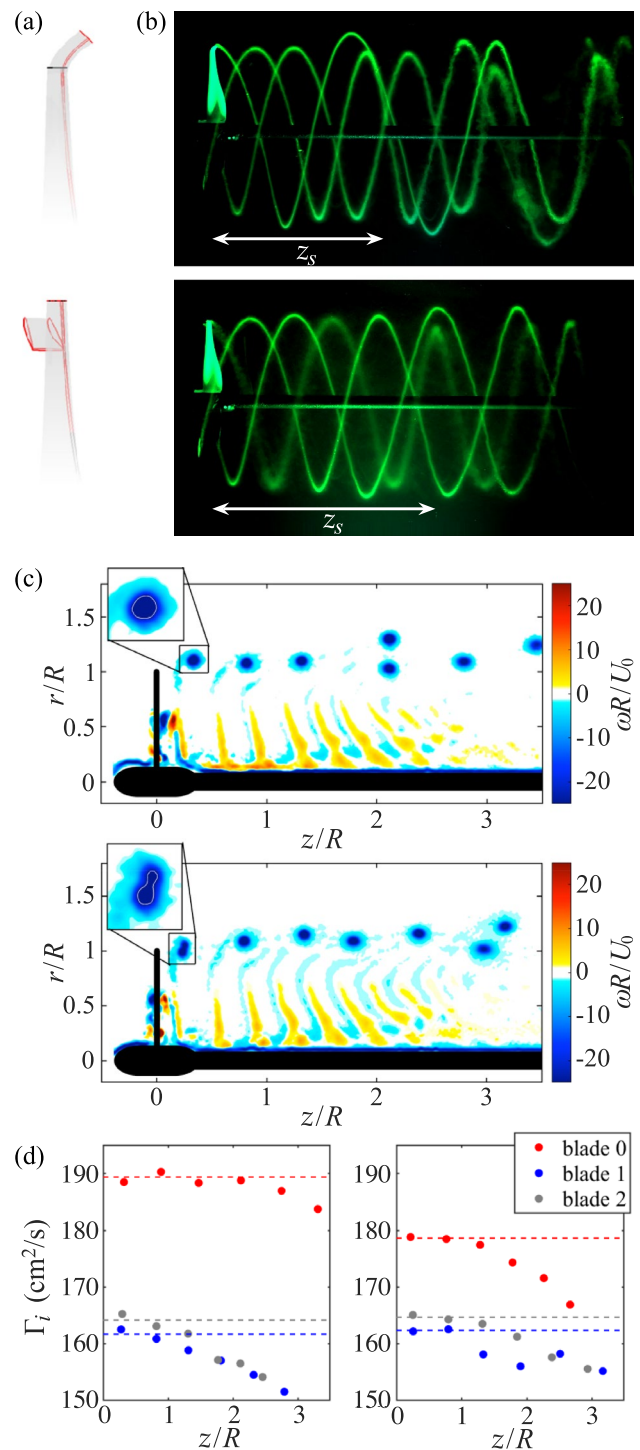


**Fig. 9** **a** Modified blades with (top) an added winglet (W in Table 1) and (bottom) an added fin (F in Table 1). Only blade tips are shown for clarity. The corresponding visualizations are shown in **b** with leapfrogging distance ( $z_s$ ) indicated, and the vorticity fields from the PIV data are shown in **c**. The insets show zoomed-in views of the most recently shed vortices from the modified blades. White contour lines at  $\omega R/U_0 = -25$  highlight the vortex shape differences between the two cases. **d** Tip vortex circulation for the winglet (left) and fin (right) cases, where blade 0 is the modified blade

rotation were measured for the asymmetric cases than the symmetric case. The vortex shed from blade W (in the blade 0 position in the left plot of Fig. 9d) exhibits significantly higher circulation values than the vortices shed from the other two blades. This circulation increase is related to the length change of the blade. In all the configurations tested, a radial extension causes the tip vortex circulation to increase, while a radial shortening reduces the tip vortex circulation. In general, tip vortex circulation is determined by the chord length, the incident velocity magnitude, and the angle of attack experienced by the blade. A radial extension causes the blade tip to experience a larger incident azimuthal velocity due to rotor rotation, but this effect is cancelled out by the reduction in chord length included in the extrapolated blade design (Sect. 2.2). Therefore, the main reason for the circulation increase is the change in angle of attack. This change is caused by the fact that the extended part of the blade is at a larger radial position where the rotor induction is lower, so it experiences a larger axial velocity. The increase in axial velocity increases the angle of attack, increasing the circulation of the shed vortex. When a winglet is used to extend the blade, the factors influencing the circulation of the tip vortex become more complex, as the blade tip is no longer perpendicular to the inflow. Still, increased circulation of the tip vortex shed from blade W is observed. The tip vortex shed from blade F also exhibits increased circulation (in the blade 0 position in the right plot of Fig. 9d). Consistent with the observations of Schröder et al. (2021, 2022), this increase is caused by the additional circulation shed from the fin, which merges with the vortex shed from the blade tip. Though asymmetries in both position and circulation of the tip vortices influence the evolution speed of the pairing instability, the findings of Abraham et al. (2023) show that a displacement of 10–15% of  $h$  along the positive strain direction reduces the leapfrogging distance more than a circulation increase of 10–15%. Therefore, the vortex displacements induced by the blade devices are primarily responsible for the short leapfrogging distances observed in these two configurations.

## 4 Conclusions

The current study experimentally investigates the effects of different types of asymmetries on the development of the helical tip vortex system in the wake of a three-bladed rotor. Rotor asymmetry is introduced by replacing one or two of the blades with slightly modified versions, perturbing the tip vortices and triggering the global pairing instability of the interlaced helical vortex system. The effectiveness of the perturbations is compared using the distance from the rotor plane where adjacent vortex loops swap positions, or the leapfrogging distance. The 14 configurations tested

yield leapfrogging distances ranging from 4.1 to 1.8 times the rotor radius, for the baseline (symmetric) case and the most perturbed case, respectively. A few of these 14 configurations are discussed in more detail, highlighting differences and similarities between certain cases. First, the similarity between azimuthal and axial displacements is attributed to their analogous effects on the helical geometry of the system. Next, the effect of displacement direction is investigated. Large discrepancies between equal-magnitude perturbations are shown to relate to the strain field generated by co-rotating vortices. Finally, the impacts of blade devices such as winglets and fins on the tip vortex behavior are explored.

The findings of the current study can be used to develop innovative rotor designs to passively accelerate tip vortex breakdown and mitigate the detrimental effects of the wake. Based on the results of the experiments presented here, even a small rotor asymmetry significantly perturbs the wake. Blades that displace the tip vortex in the direction of positive strain are shown to be especially effective, whether this perturbation is implemented using a full blade modification or through the addition of a device such as a winglet or fin. The magnitude of these perturbations scale with the vortex spacing, which is larger relative to the radius in the current experiments than in the wake of real wind turbine rotors due to the difference in tip speed ratios (typically between 6 and 8, compared to 3 in the current study). Therefore, to achieve the same perturbation magnitudes on a real wind turbine, smaller blade modifications of only 1–2% of rotor radius would be required.

Still, many questions remain to be addressed before this technology can be used on a real rotor. First, additional experiments are underway to investigate the effects of turbulence on tip vortex breakdown. In the water channel used in the current study, the turbulence intensity is very low ( $< 1\%$ ). This lack of turbulence could be responsible for the absence of vortex breakdown in the current experiments. In addition, the current study characterizes the wake, but does not quantify the impacts of the modified wake on structures in the downstream flow. The experimental setup does not allow for additional rotors to be mounted in the wake of the rotor, but high-fidelity simulations are underway to quantify the effects of an asymmetric rotor wake on the structural loading and power generation of a downstream wind turbine (Ramos-García et al. 2023). Finally, asymmetry is expected to generate fluctuating loads on the support structure and the asymmetric rotor itself. The possibility of compensating for these additional forces, e.g., with a counterweight, should be explored to enable the practical implementation of asymmetric rotors.

**Acknowledgements** The authors gratefully acknowledge the contributions of Eric Bertrand to the design and manufacture of the rotor.

**Author contributions** AA analyzed the experimental data and wrote the manuscript. TL edited the manuscript and acquired the funding. Both AA and TL conducted the experiments.

**Funding** This work was supported by the technology transfer company SATT Sud-Est (Marseille).

**Availability of data and materials** Data and codes are available on request from the authors.

## Declarations

**Conflict of interest** The authors have no competing interests to declare.

## References

- Abraham A, Castillo-Castellanos A, Leweke T (2023) Simplified model for helical vortex dynamics in the wake of an asymmetric rotor. *Flow* 3:5. <https://doi.org/10.1017/flo.2022.33>
- Alfredsson PH, Dahlberg JA (1979) A preliminary wind tunnel study of windmill wake dispersion in various flow conditions. Technical report, FFA, Stockholm, Sweden
- Bhagwat MJ, Leishman JG (2000) Stability analysis of helicopter rotor wakes in axial flight. *J Am Helicopter Soc* 45(3):165–178. <https://doi.org/10.4050/JAHS.45.165>
- Brown K, Houck D, Maniaci D, Westergaard C, Kelley C (2022) Accelerated wind-turbine wake recovery through actuation of the tip-vortex instability. *AIAA J* 60(5):3298–3310. <https://doi.org/10.2514/1.j060772>
- Felli M, Camussi R, Di Felice F (2011) Mechanisms of evolution of the propeller wake in the transition and far fields. *J Fluid Mech* 682:5–53. <https://doi.org/10.1017/jfm.2011.150>
- Formlabs Inc.: Rigid 10K Technical Data Sheet. <https://formlabs-media.formlabs.com/datasheets/2001479-TDS-ENUS-0.pdf> (2022)
- Gerontakos P, Lee T (2006) Effects of winglet dihedral on a tip vortex. *J Aircr* 43(1):117–124. <https://doi.org/10.2514/1.14052>
- Glauert H (1935) Airplane propellers. In: Durand WF (ed) *Aerodynamic Theory*. Springer, New York, pp 169–360. [https://doi.org/10.1007/978-3-642-91487-4\\_3](https://doi.org/10.1007/978-3-642-91487-4_3)
- Gupta BP, Loewy RG (1974) Theoretical analysis of the aerodynamic stability of multiple, interdigitated helical vortices. *AIAA J* 12(10):1381–1387. <https://doi.org/10.2514/3.49493>
- Hodgkin A, Laizet S, Deskos G (2022) Numerical investigation of the influence of shear and thermal stratification on the wind turbine tip-vortex stability. *Wind Energy* 25:1270–1289. <https://doi.org/10.1002/we.2728>
- Huang X, Alavi Moghadam SM, Meysonnat PS, Meinke M, Schröder W (2019) Numerical analysis of the effect of flaps on the tip vortex of a wind turbine blade. *Int J Heat Fluid Flow* 77:336–351. <https://doi.org/10.1016/j.ijheatfluidflow.2019.05.004>
- Ivanell S, Mikkelsen R, Sørensen JN, Henningson D (2010) Stability analysis of the tip vortices of a wind turbine. *Wind Energy* 13:705–715
- Kleine VG, Franceschini L, Carmo BS, Hanifi A, Henningson D (2022) The stability of wakes of floating wind turbines. *Phys Fluids* 34:074106. <https://doi.org/10.1063/5.0092267>
- Lee JCY, Fields MJ (2021) An overview of wind-energy-production prediction bias, losses, and uncertainties. *Wind Energy Sci* 6(2):311–365. <https://doi.org/10.5194/wes-6-311-2021>
- Leweke T, Williamson CHK (1998) Cooperative elliptic instability of a vortex pair. *J Fluid Mech* 360:85–119. <https://doi.org/10.1017/S0022112097008331>
- Leweke T, Quaranta HU, Bolnot H, Blanco-Rodríguez FJ, Le Dizès S (2014) Long- and short-wave instabilities in helical vortices. *J Phys: Conf Series* 524(1):012154. <https://doi.org/10.1088/1742-6596/524/1/012154>
- Leweke T, Le Dizès S, Williamson CHK (2016) Dynamics and Instabilities of Vortex Pairs. *Annu Rev Fluid Mech* 48:507–541. <https://doi.org/10.1146/annurev-fluid-122414-034558>
- Lignarolo LEM, Ragni D, Scarano F, Simão Ferreira CJ, Van Bussel GJW (2015) Tip-vortex instability and turbulent mixing in wind-turbine wakes. *J Fluid Mech* 781:467–493. <https://doi.org/10.1017/jfm.2015.470>
- Marten D, Paschereit CO, Huang X, Meinke M, Schröder W, Müller J, Oberleithner K (2020) Predicting wind turbine wake breakdown using a free vortex wake code. *AIAA J* 58(11):4672–4685. <https://doi.org/10.2514/1.J058308>
- Meunier P, Leweke T (2003) Analysis and treatment of errors due to high velocity gradients in particle image velocimetry. *Exp Fluids* 35:408–421. <https://doi.org/10.1007/s00348-003-0673-2>
- Meyers J, Bottasso C, Dykes K, Fleming P, Gebraad P, Giebel G, Göçmen T, Van Wingerden J-W (2022) Wind farm flow control: prospects and challenges. *Wind Energy Sci* 7(6):2271–2306. <https://doi.org/10.5194/wes-7-2271-2022>
- Nemes A, Lo Jacono D, Blackburn HM, Sheridan J (2015) Mutual inductance of two helical vortices. *J Fluid Mech* 774:298–310. <https://doi.org/10.1017/jfm.2015.288>
- Okulov VL, Sørensen JN (2007) Stability of helical tip vortices in a rotor far wake. *J Fluid Mech* 576:1–25. <https://doi.org/10.1017/jfm.2011.277>
- Ostovan Y, Akpolat MT, Uzol O (2019) Experimental investigation of the effects of winglets on the tip vortex behavior of a model horizontal axis wind turbine using particle image velocimetry. *J Solar Energy Eng* 141:011006. <https://doi.org/10.1115/1.4041154>
- Quaranta HU, Bolnot H, Leweke T (2015) Long-wave instability of a helical vortex. *J Fluid Mech* 780:687–716. <https://doi.org/10.1017/jfm.2015.479>
- Quaranta HU, Brynjell-Rahkola M, Leweke T, Henningson DS (2019) Local and global pairing instabilities of two interlaced helical vortices. *J Fluid Mech* 863:927–955. <https://doi.org/10.1017/jfm.2018.904>
- Ramos-García N, Abraham A, Leweke T, Sørensen JN (2023) Multi-fidelity vortex simulations of rotor flows: validation against detailed wake measurements. *Comput Fluids* 255:105790. <https://doi.org/10.1016/j.compfluid.2023.105790>
- Sarmast S, Dadfar R, Mikkelsen RF, Schlatter P, Ivanell S, Sørensen JN, Henningson DS (2014) Mutual inductance instability of the tip vortices behind a wind turbine. *J Fluid Mech* 755:705–731. <https://doi.org/10.1017/jfm.2014.326>
- Schröder D, Leweke T, Hörschemeyer R, Stumpf E (2021) Experiments on helical vortex pairs in the wake of a rotor. In: *AIAA Paper* 2021, p 1088. <https://doi.org/10.2514/6.2021-1088>
- Schröder D, Leweke T, Hörschemeyer R, Stumpf E (2022) Generation of a wingtip vortex pair using a pressure-side fin. *Aerosp Sci Technol* 130:107860. <https://doi.org/10.1016/j.ast.2022.107860>
- Selig MS, Lyon CA, Giguère P, Ninham CN, Guglielmo JJ (1996) Summary of low-speed airfoil data, vol 2. SoarTech, Virginia Beach
- Sørensen JN (2011) Instability of helical tip vortices in rotor wakes. *J Fluid Mech* 682:1–4. <https://doi.org/10.1017/jfm.2011.277>

Widnall SE (1972) The stability of a helical vortex filament. *J Fluid Mech* 54(4):641–663. <https://doi.org/10.1017/S0022112072000928>

**Publisher's Note** Springer Nature remains neutral with regard to jurisdictional claims in published maps and institutional affiliations.

Springer Nature or its licensor (e.g. a society or other partner) holds exclusive rights to this article under a publishing agreement with the author(s) or other rightsholder(s); author self-archiving of the accepted manuscript version of this article is solely governed by the terms of such publishing agreement and applicable law.